Non-Destructive Analysis of Concentration Profiles in Turbid Media using micro-SORS: A Physical Model

Chiara Castiglioni[a], Alessandra Botteon[a,b*], Claudia Conti[b], Matteo Tommasini[a], Pavel Matousek[c]

a. Department of Chemistry, Materials and Chemical Engineering Giulio Natta, Politecnico di Milano, Milan, Italy

b. National Research Council (CNR), Institute of Heritage Science (ISPC), Milan, Italy

c. Central Laser Facility, Research Complex at Harwell, STFC Rutherford Appleton Laboratory, UKRI, Harwell Oxford, UK

*Corresponding author: Alessandra Botteon, alessandra.botteon@cnr.it

Key words: micro-SORS; diffusion; Cultural Heritage; photons propagation; concentration profile

Abstract

We introduce an analytical physical description of micro-Spatially Offset Raman Spectroscopy (micro-SORS) experiments in turbid samples with a special emphasis on studying the penetration depth of chemical species (agents) into a matrix. Such samples exhibit varying concentration gradients with depth. The experiments aim at yielding the variations (trends) of the Raman intensity ratio of the agent and matrix marker bands, $H(X)$, with increasing micro-SORS defocusing distance (X). The physical model shows that $H(X)$ can be expressed as a function of the concentration profiles of the analytes. The analysis makes use of Monte Carlo simulation results of the propagation of photons in turbid media. Despite the introduced approximations, the obtained formulas provide an insightful tool that allows justifying the observed trends and facilitates the interpretation of micro-SORS data and systematic comparison among different samples. Basic comparison with previously published experimental micro-SORS data indicates good consistency. The obtained relationships could also be useful for a semi-quantitative estimate of concentration profiles in unknown samples.

1. Introduction

The study of the concentration gradient of an agent which diffuses in turbid media is a topic transcending many fields of materials science. For instance, in the field of semiconductors it is relevant in the study of the diffusion of dopants into silicon wafers; [1] in solar cells technology it is of interest for the study of the diffusion of alkali ions from the glass into the electrode films; [2] in the pharmaceutical field it is pertinent in studying the absorption of drugs or moisture in tablets,[3] drug release [4-5] and drug diffusion in human skin. [6] Overall, the knowledge of the diffusion profiles and associated dynamics of the process is crucial for the understanding of complex mechanisms underlying the diffusion processes, which strongly influence the properties of many materials.

In Cultural Heritage the diffusion phenomenon is present, for instance, when a conservation product is applied on a decayed substrate (stones, plasters, mural paintings, paintings, etc.). The aim of such treatment is to restore, or at least to contain, the natural decay processes of the artwork, and the knowledge of the concentration profile of the product inside the porous matrix is mandatory for investigating the physical-chemical interaction between these, and consequently, for evaluating the effects of the treatment. [17-24] Other situations that involve diffusion processes in Cultural Heritage include the absorption of dye solutions or pigment suspensions (*e.g.*, watercolour absorbed in a paper substrate) and the diffusion of solvents used for cleaning. The knowledge of the penetration depth of these agents is relevant for characterizing the artwork and for monitoring the (unwanted) diffusion of the solvents during the cleaning procedure. [25]

Recently, a Raman spectroscopy technique, micro-Spatially Offset Raman Spectroscopy (micro-SORS) has been proposed for obtaining the diffusion profiles of an agent into a turbid (diffusely scattering) matrix, with a special interest to Cultural Heritage applications. [26-28] The method is based on the physical concept that deep Raman photons, carrying chemical information from different depths below the surface, emerge laterally on sample surface; their acquisition permits to discriminate the molecular composition of the surface from that below it – for a detailed description of the method and underlying processes see [29-30] and references therein.

In its basic form (called defocusing micro-SORS), micro-SORS entails the acquisition of a sequence of Raman spectra at different sample positions along the z-axis facilitating the detection of Raman photons originating from different locations within the sample volume. [31] Besides the high chemical specificity and sensitivity, a major advantage of micro-SORS stems from its non-invasive nature. The acquisition of the deep Raman photons, and consequently the assessment of the diffusion profiles, is obtained without resorting to destructive methods, as required in cross sectional analysis, performed directly at the surface of the intact material. This feature is essential, notably in the Cultural Heritage field, where, for evident reasons the development of non-invasive methods is among the key research topics.

Extensive studies have recently demonstrated the applicability of micro-SORS to these complex situations. Mock-up samples mimicking the absorption of solvents used for cleaning, [26-27] the diffusion of an organic polymer, [26] an inorganic treatment used in conservation and a pigment suspension [28] have been tested with micro-SORS, using different matrices. Normalized intensity ratios between the marker bands of the agent and that of the matrix, $H(X)$, were used to calculate the slopes $dH(X)/dX$ *vs*. defocusing distance X. This parameter was found to be related to the actual penetration depth of the agent, demonstrating the capability of micro-SORS to differentiate samples with different penetration depths. (The penetration depth is defined as a depth at which the concentration of the penetrating agent decreases to 1/e of its near surface value).[28]

To support the interpretation of micro-SORS data and the systematic comparison of different samples a further major step is needed involving the development of a physical model able to analytically justify the remarkable outcomes achieved so far by micro-SORS experiments. Despite the relevance, this subject is still rather unexplored in literature, but it can rely on a series of available theoretical results. Notably, the Monte Carlo method has been used to numerically simulate the photon paths in SORS experiments [32] and to study the micro-SORS signal dependence on the degree of spatial offset [33-34] and defocusing.[33-35] Moreover, simulations have been carried out of deep Raman photons collection with a fluorescence top layer using defocusing and full micro-SORS variants. [36] Here we propose a physical model that combines the description of the Raman response of the chemical species with the results of Monte Carlo simulations that provided the description of the probed depth in micro-SORS measurements in a turbid matrix.

Our model aims at the description of real situations often encountered in Cultural heritage materials. For instance, when consolidants, protectives, solvents or coloured suspensions are applied on the surface of absorbing matrixes such as plasters, stones, or paper, a continuous concentration gradient develops in the sample, which results from the diffusion of the agent within the matrix.

We first consider a generic system where an agent is embedded in a non-transparent matrix, creating a concentration gradient from the surface to the inner portion of the material. Both chemical species (agent and matrix, $S1,\ S2$) can change their absolute concentration with depth. Analytic relationships valid for any concentration profiles, $C^{Sk}(z)$, are derived. The model is then applied to systems reflecting situations encountered in Cultural Heritage: i) the agent possesses a (continuous) concentration profile whereas the matrix concentration is constant (e.g a consolidant that diffuses in a porous stone), and ii) the agent/matrix mixture forms finite thickness layers (multi-layered system) with constant relative concentration that gives a stepwise concentration profile of the two analytes (e.g superimposed paint layers).

The model was finally tested on a sample that exhibits both i) and ii) features, and is made of two-layers with constant concentration profile of the matrix itself, simulating a pigment suspension diffused in a paper substrate with a stepwise concentration profile. Such types of samples were previously investigated with micro-SORS,[28] and the model output has been compared with experimental data collected in this work.

2. Derivation of the model

The aim of the model is to obtain equations that describe, in terms of relevant physical quantities, the output of a micro-SORS experiment carried out on a sample characterized by the presence of two analytes with variable relative concentration with different depths. We indicate these two species with the symbols $S1$ and $S2$; typically, $S1$ is the agent and $S2$ is the matrix. The model can be applied to samples having both a constant and a variable concentration of the matrix, to samples with a continuous concentration gradient, and to layered samples, consisting of a mixture of the two analytes creating layers with different relative concentrations. Such situations are commonly found in several art-relevant materials, for example, treated stones having a product diffusion gradient, with the matrix being either constant or variable in concentration, and superimposed paint layers (stratigraphies).

The system considered for the development of the model is described as a semi-infinite volume, with a flat interface with air (Figure 1). The experimental set-up considered is typical of a defocusing micro-SORS experiment with incidence of the laser beam normal to the sample surface and a backscattering collection geometry. The concentration of the two analytes (moles/volume) is described by the functions $C^{S1}(z), C^{S2}(z)$ varying along the z direction (depth) and this is assumed to be constant in the x, y plane. In the following, z represents the depth into the sample ($z = 0$ at the interface, z increases with depth (see Fig. 1)). We assume the air/sample interface is flat. The coordinate X describes the defocusing: the displacement of the microscope objective away from the sample surface – X increases with increasing micro-SORS defocusing distance. We also assume that neither laser nor Raman photons are absorbed by the matrix or agent, which is a reasonable assumption with common near-infrared micro-SORS probing.

We consider a pair of different analytes, and we assume that $S1$ (agent) and $S2$ (matrix) exhibit characteristic Raman marker bands, so that their relative amount can be monitored by following, during the micro-SORS experiment, the evolution with defocusing distance (X) of the intensity ratio of the two Raman bands, namely $R(X) = \frac{A^{S1}(X)}{A^{S2}(X)}$. Often, instead of $R(X)$, the normalized intensity ratio $H(X) = \frac{R(X)}{R(X^0)}$ is reported and analyzed where X^0 is a given selected defocusing distance. The reference defocusing value X^0 may correspond either to the optical focus ($X_f = X^0$) or to a reference distance further away from it ($X_0 > X_f$). The choice of the suitable X^0 value depends on the characteristics of the depth distribution of the analytes. According to ref.,[28] real samples can be affected by local (unwanted or unexpected) fluctuation of the concentration profiles: in this case it is preferable to perform a normalization to the intensity ratio obtained at a selected threshold defocusing value. In fact, the increase of the defocusing distance compensates for the possible non-homogeneous layer composition, due to the intrinsic averaging ability of defocusing, provided by the enlargement of the laser incidence and Raman collection areas.

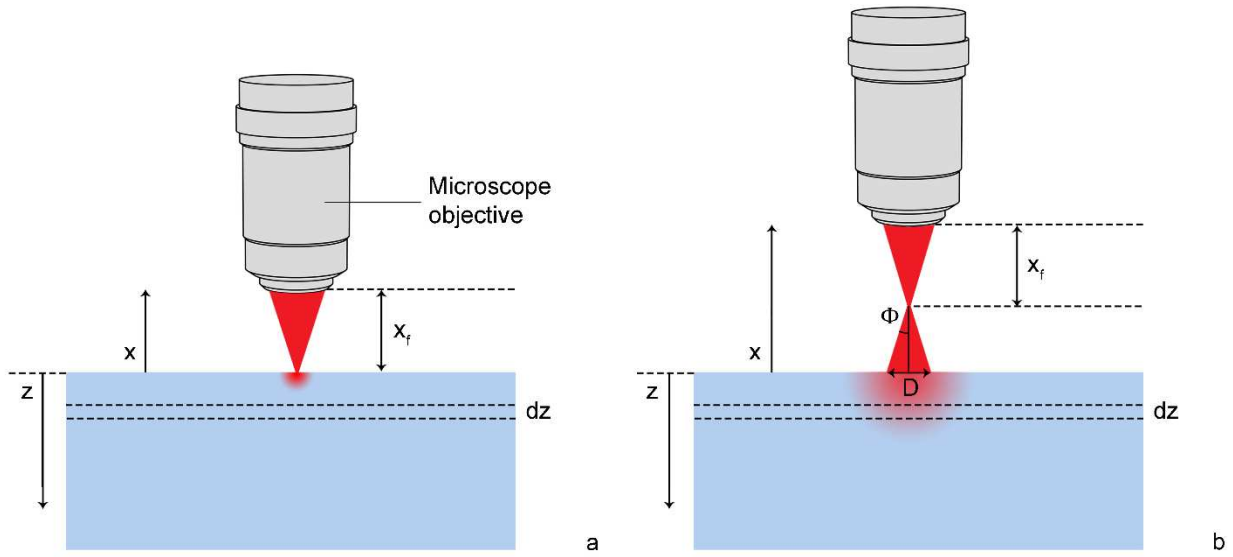

Figure 1. *Sketch of the experimental micro-SORS set-up considered for developing the model. X measures the distance between the microscope objective and the sample surface and z the depth in the sample. Panel a: imaged set-up. Panel b: Defocused (micro-SORS) set-up.* X_f *is the microscope focal distance.*

The model is based on the following hypothesis about the Raman intensity (photons counts) $A^{Sk}(X)$ from a given analyte Sk; $A^{Sk}(X)$ essentially depends on the following quantities:

1. the effective volume probed by the photons at the given defocusing step X. Notice that this volume effectively monotonically increases with the defocusing distance. Since the meaning of volume *probed* comprises also the effective ability to detect Raman photons from that volume, it depends both on the propagation of the laser photons in the sample and on the "escaping" capability of the scattered Raman photons. Notice that only a fraction of scattered Raman photons will be able to reach the collection zone on sample surface and this ability will depend on the specific position $\boldsymbol{P} = (x, y, z)$ in the sample from which they start diffusing.
2. the probed quantity of analyte (= moles of the analyte within the probed volume). Notice that this amount depends on the concentration profile $C^{S1}(z)$ and on the volume probed at the defocusing distance X.
3. the Raman scattering cross section corresponding to the selected Raman marker band of Sk
4. the incident laser power.

With reference to Fig. 1, let us first consider a slice inside the material, placed at a given depth z, and whose thickness is *dz*. We can write the contribution to the photon counts due to the Raman scattering from this depth:

$$dn^X(z) = \left(\rho_0^X \int_{-\infty}^{+\infty}\int_{-\infty}^{+\infty} C^{S1}(z)\sigma^{S1} g^X(x,y,z)\,dx\,dy\right)dz = \rho_0^X C^{S1}(z)\,\sigma^{S1}dz \int_{-\infty}^{+\infty}\int_{-\infty}^{+\infty} g^X(x,y,z)\,dx\,dy$$

(eq. 1)

The meaning of the symbols in eq. 1 is:

$$\sigma^{S1} = \textit{absolute Raman cross section of the selected marker band of S1}$$

$$\rho_0^X = \textit{equilibrated laser photon density at surface at the centre of the laser beam,}$$

$$\textit{proportional to the laser power}$$

$$g^X(x,y,z) = p^X(x,y,z)\,f^X(x,y,z)$$

$$\rho_0^X\, p^X(x,y,z) = \textit{local density of laser photons at point } \boldsymbol{P} = (x,y,z)$$

$$f^X(x,y,z) = \textit{escape factor of scattered photons in } \boldsymbol{P}$$

The quantity:

$$\rho_0^X\, g^X(x,y,z) = \rho_0^X\, p^X(x,y,z)\, f^X(x,y,z)$$

describes the density of the Raman photons, scattered at a given point in the sample, that can reach the detection aperture at sample surface (for unitary analyte concentration and unitary absolute Raman cross section).

The considered set-up is characterized by rotational symmetry, with its axis coinciding with the laser beam propagation axis (*z*) that is assumed to be orthogonal to the surface of the sample. We can define an average G^X factor:

$$G^X(z) = \int_{-\infty}^{+\infty} dx \int_{-\infty}^{+\infty} dy\, g^X(x,y,z) = \int_0^{2\pi} d\theta \int_0^{+\infty} dr\,[r\, g^X(r,z)] = 2\pi \int_0^{+\infty} dr\,[r\, g^X(r,z)] \qquad \text{(eq. 2)}$$

where the last two equalities make explicit use of the rotational symmetry around the z axis (in cylindrical coordinates r, z, θ). According to eq. 2, $\rho_0^X G^X(z)dz$ describes the average density of scattered photons coming from depth z, for a fixed defocusing length X.

Introducing the molar concentration of $S1$ in a layer of thickness dz located at depth z, and its absolute Raman cross section, the number of Raman photons arriving at the surface from the depth z is

$$dn^X(z) = \rho_0^X\, C^{S1}(z)\, \sigma^{S1}\, G^X(z)\, dz \qquad \text{(eq. 3)}$$

The total photon counts (i.e., the Raman intensity of the marker band of *e.g.*, $S1$) are obtained by integration over z:

$$A^{S1}(X) = \rho_0^X\, \sigma^{S1} \int_0^{+\infty} C^{S1}(z)\, G^X(z)\, dz \qquad \text{(eq. 4)}$$

In a similar way, we can write the expression for the intensity of the marker Raman band of the second analyte, $S2$:

$$A^{S2}(X) = \rho_0^X \ \sigma^{S2} \int_0^{+\infty} C^{S2}(z)\, G^X(z)\, dz \qquad \text{(eq. 5)}$$

By using eq. 4 and eq. 5 we can directly write the intensity ratio $R(X)$:

$$R(X) = \frac{A^{S1}(X)}{A^{S2}(X)} = \frac{\rho_0^X \ \sigma^{S1}}{\rho_0^X \ \sigma^{S2}} \times \frac{\int_0^{+\infty} C^{S1}(z)\, G^X(z)\, dz}{\int_0^{+\infty} C^{S2}(z)\, G^X(z)\, dz} = \frac{\sigma^{S1}}{\sigma^{S2}} \times \frac{\int_0^{+\infty} C^{S1}(z)\, G^X(z)\, dz}{\int_0^{+\infty} C^{S2}(z)\, G^X(z)\, dz}$$

(eq. 6)

From eq. 6 we can deduce that:

i. $R(X)$ does not depend on the incident photon density.

ii. In eq. 6 we can substitute the molar concentration $C^{Sk}(z)$ (moles/volume) with the molar fractions ($c^{Sk}(z)$) of the two analytes: $c^{Sk}(z) = C^{Sk}(z)/M$, where $M = M^{S1} + M^{S2}$ corresponds to the total moles of analytes per unit volume. Indeed, M simplifies when substituting $c^{Sk}(z)$ into eq. 6.
Hence in eq. 6 and in the following expressions we can read the symbol $C^{Si}(z)$ both as molar concentration and as molar fraction. This can be useful while comparing our theoretical predictions with experiments on real samples.

$R(X^0)$ is simply obtained from eq. 6, evaluated at $X = X^0$ (imaged set-up distance, or reference threshold defocusing distance)

$$R(X^0) = \frac{\sigma^{S1}}{\sigma^{S2}} \times \frac{\int_0^{+\infty} C^{S1}(z)\, G^0(z)\, dz}{\int_0^{+\infty} C^{S2}(z)\, G^0(z)\, dz} \qquad \text{(eq. 7)}$$

Accordingly:

$$H(X) = \frac{R(X)}{R(X^0)} = \frac{(\int_0^{+\infty} C^{S1}(z)\, G^X(z)\, dz) \times (\int_0^{+\infty} C^{S2}(z)\, G^0(z)\, dz)}{(\int_0^{+\infty} C^{S2}(z)\, G^X(z)\, dz) \times (\int_0^{+\infty} C^{S1}(z)\, G^0(z)\, dz)} \qquad \text{(eq. 8)}$$

Eq. 8 shows a very important property of $H(X)$: thanks to the normalization with respect to $R(X^0)$, *H(X)* does not depend on the ratio of the absolute Raman intensities of the two marker bands ($\frac{\sigma^{S1}}{\sigma^{S2}}$).

$G^X(z)$ is a property of the material, and in the case of analytes dispersed in a matrix it is in general expected to depend on the optical properties of the matrix. The knowledge (or a modelling) of $G^X(z)$ should allow to extract concentration profiles of the analytes, $C^{Sk}(z)$, by fitting the experimental micro-SORS normalized ratios $H(X)$.

3. Application of the model to selected cases

In Section 4, a method to obtain a suitable analytic expression for the $G^X(z)$ function, based on Monte Carlo simulation of the photons propagation in a semi-infinite, non-absorbing turbid medium, will be presented. Here, eq. 8 will be simplified for some special cases that highlight the behaviour of $H(X)$ in physically relevant situations.

3.1 Case I: C^{S2} is constant along the whole material thickness $C^{S2}(z) = \overline{C^{S2}}$

This case corresponds to a common situation, where an agent $S1$ is diffusing in a matrix $S2$ having a constant concentration, $\overline{C^{S2}}$. The expression will be derived under the assumption that the matrix density is not perturbed by the diffusing agent, which is a reasonable assumption for a porous matrix, as well as for small amounts of $S1$.

$$H(X) = \frac{(\int_0^{+\infty} C^{S1}(z)\, G^X(z)\, dz)\times\overline{C^{S2}}(\int_0^{+\infty} G^0(z)\, dz)}{\overline{C^{S2}}(\int_0^{+\infty} G^X(z)\, dz)\times(\int_0^{+\infty} C^{S1}(z)\, G^0(z)\, dz)} = \frac{(\int_0^{+\infty} C^{S1}(z)\, G^X(z)\, dz)\times(\int_0^{+\infty} G^0(z)\, dz)}{(\int_0^{+\infty} G^X(z)\, dz)\times(\int_0^{+\infty} C^{S1}(z)\, G^0(z)\, dz)}$$

(eq. 9)

Evidently, in eq. 9 the dependence on $\overline{C^{S2}}$ vanishes. More interestingly, eq. 9 shows that $H(X)$ is the same for samples where the concentration profile of $S1$ is functionally similar, i.e., $C'^{S1}(z) = K\, C^{S1}(z)$. In this case it follows that H(X) is not sensitive to the concentration value at the surface ($C^{S1}(0)$). Therefore, we can state that normalized micro-SORS intensity ratios cannot provide information on the total amount of $S1$. This predicted behaviour is experimentally proven by micro-SORS measurement on special layered samples[28] consisting of a paper sheet matrix ($S2$) soaked in a blue pigment suspension ($S1$); see Section 5 for the detailed description of the samples and the specific application of the model.

3.2 Case II. Multilayered samples (stepwise concentration profiles)

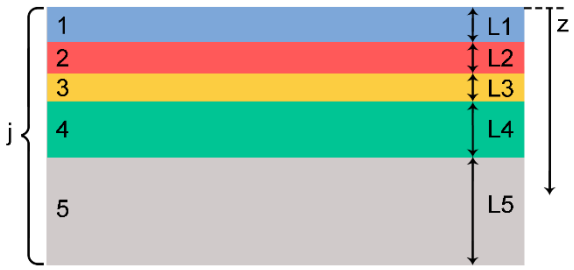

Figure 2. *Sketch of a multi-layered sample. The concentration of S1 and S2 is constant along the full thickness of each layer. j numbers the layers, with thickness L_j.*

The sample consists of N layers (j=1, 2,…N) of thickness L_j that are made of different mixtures of S1 and S2. In any given layer j each analyte ($S1$ and $S2$) has a constant concentration C_j^{Sk} (Figure 2). The interfaces between layers are flat, and are located at z values determined by the thickness of the upper layers, so the interface between layer k and layer $k+1$ is located at the depth:

$$z_k = \sum_{j=1}^{k} L_j$$

By splitting the integrals appearing in eq. 9 into N integrals that describe the contribution of each layer, we obtain:

$$H(X) = \frac{R(X)}{R(X^0)} = \frac{[\sum_k^N C_k^{S1} \times \Gamma^X(z_{k,}z_{k-1})] \times [(\sum_k^N C_k^{S2} \times \Gamma^0(z_{k,}z_{k-1})]}{[(\sum_k^N C_k^{S2} \times \Gamma^X(z_{k,}z_{k-1})] \times [(\sum_k^N C_k^{S1} \times \Gamma^0(z_{k,}z_{k-1})]} \qquad \text{(eq. 10)}$$

with:

$$\Gamma^X(z_{k,}z_{k-1}) = \int_{z_{k-1}}^{z_k} G^X(z)\, dz \qquad \text{(eq. 11)}$$

Usually, a layered sample is described by a few layers with different thicknesses and different concentrations of the two analytes. The last layer (substrate) is supposed to be made of $S2$ only, and to be of infinite thickness; hence, in this case we have (for $k = N, L_k = +\infty$):

$$\Gamma^X(z_{N-1}, z_N) = \int_{z_{N-1}}^{+\infty} G^X(z)\, dz \qquad \text{(eq. 12)}$$

If we consider the layer k of thickness L_k, by using eq. 11 we can introduce the average value of G^X within the layer, as follows:

$$\Gamma^X(z_{k,}z_{k-1}) = < G^X(z) >_k \; L_k \qquad \text{(eq. 13)}$$

where

$$< G^X(z) >_k = \frac{1}{L_k} \int_{z_{k-1}}^{z_k} G^X(z)\, dz \qquad \text{(eq. 14)}$$

In the following Section we show how the $G^X(z)$ function, which is expected to be a decreasing function of z, also depending on the defocusing X, can be effectively determined from Monte Carlo simulations. Once the $G^X(z)$ function is defined, one can evaluate the integrals $\Gamma^X(z_{k,}z_{k-1})$, thus obtaining a relationship $H(X) = f(C_k^{S1}, L_k)$ that depends just on the concentration of the S1 species within the layers and the thickness of the layers.

4. Determination of the function $G^X(z)$

3D Monte Carlo simulations were used to evaluate the probed depth with defocusing micro-SORS within a diffusely scattering matrix. The code was described in detail elsewhere.[32-33] Briefly, laser and Raman photons were propagated through a matrix with a step size equal to the photon transport length, [37] l_t. After each step

their direction was randomised. (The transport length is related to the reduced scattering coefficient (μ_s') of the matrix through $l_t = 1/\mu_s'$)

The numerical code was written in Mathematica 9.0.1.0 (Wolfram Research). 2,000,000 photons were propagated simultaneously over 10,000 steps with a step size of $l_t = 0.2$ mm. The sample was assumed to be non-absorbing at both the laser and Raman photon wavelengths and semi-infinite in depth and in lateral dimensions. The incident laser photons were initially placed at a depth equal to the photon transport length l_t and uniformly distributed within the illumination area of diameter $D = 6$ mm. The locations of laser-to-Raman photon conversion points inside the sample were recorded during the simulations. [38] The Raman photons were detected through the same area as the illumination zone. Only these detected Raman photons was considered in the analysis. The origin of Raman photons was closely inspected within a depth range of 0 - 4 mm. This range was subdivided into 10 segments, each 0.4-mm thick and the detected Raman photons generated in each segment were summed up. This yielded the depth dependence of originating Raman photons detected in this specific geometry. This dependence is shown in Figure 3.

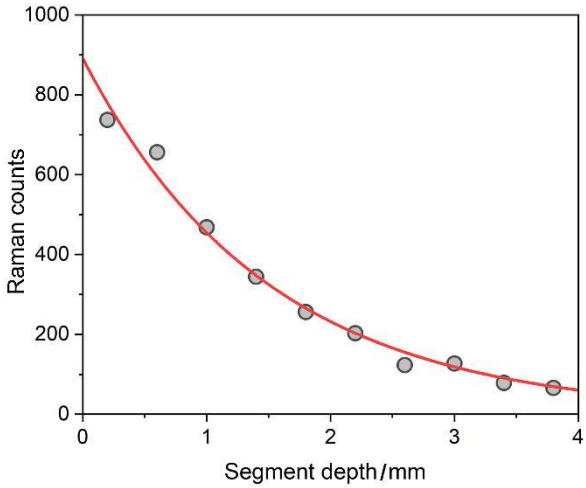

Figure 3. *Depth dependence of detected Raman photons (grey dots - Monte Carlo simulations) fitted to a single exponential decay function (red line).*

Figure 3 also illustrates that the dependence of detected Raman photons on their originating depth can be satisfactorily modelled using a single exponential decay function (the fit was performed with OriginPro 2018 SR1).

$$\Delta R = A \times \mathrm{e}^{-\frac{z}{\lambda}} \qquad \text{(eq. 15)}$$

where ΔR is the Raman intensity contribution from a layer at depth z, A is the Raman contribution from the surface layer (z = 0), z is the depth and λ is the characteristic depth from which the Raman signal originates.

The fit yields a value of λ = 1.487 mm. This means that, at this (characteristic) depth, the Raman signal contribution drops from that of the surface layer by a factor $1/\mathrm{e}$.

A further assumption can be made by postulating that the characteristic penetration depth, λ, scales linearly with the diameter of the illumination and collection zones, D. This is a crude simplification, but it is supported by analogous Monte Carlo simulations for full micro-SORS geometry presented in Fig. 2B in reference [38] indicating that the depth from which the Raman signal originates could be crudely approximated with a linear dependence on the spatial offset (note: the spatial offset is analogous to the defocusing illumination and collection diameter, D used here). This assumes a high turbidity medium with the photon transport length being much smaller than the laser beam diameter.

As such we can write

$$\lambda = D \times k$$

where k is a constant, namely

$$k = \frac{\lambda}{D} = \frac{1.487\ mm}{6\ mm} \sim 0.2478$$

And from the above it therefore follows that

$$G(z) = G_0 e^{-\frac{z}{0.2478D}} \qquad \text{(eq. 16)}$$

According to eq. 16 the defocusing is described by the diameter D of the illumination/collection zone. We can explicitly introduce the defocusing parameter X considering the objective half aperture Φ: by simple geometric optics, we have:

$$D = 2(X\text{-}X_f)\ \tan(\Phi) = 2(X\text{-}X_f)\ \tan(\Phi)$$

Where X_f identifies the location of the objective at the imaged position (see Figure 1). Therefore:

$$G^X(z) = G_0^X\, e^{-\frac{z}{\gamma(X\text{-}X_f)}} \qquad \text{(eq. 17)}$$

with:

$$\gamma = 2 \times 0.2478 \tan(\Phi) \qquad \text{(eq. 18)}$$

5. A test case: pigment suspension in a paper substrate

We simplify eq. 10 for the case illustrated in Figure 4, adopting the hypothesis of Case I, Section 3, namely the matrix (paper) has uniform concentration ($C^{S2} = C$). The aim is to test the effectiveness of the relationship developed in describing the experimental findings from micro-SORS measurement on simple mock-up samples previously analyzed with defocusing micro-SORS. [28]

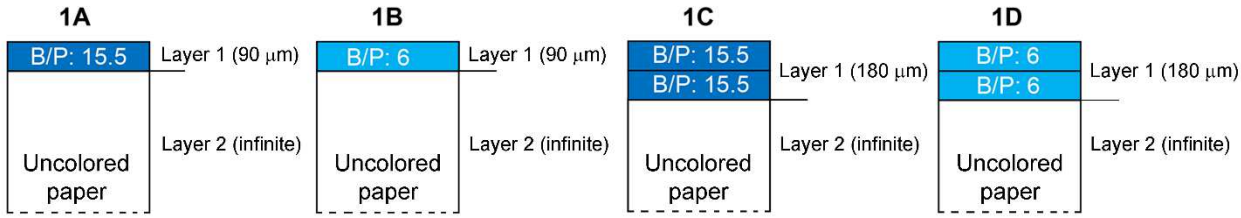

Figure 4. *Cross-section view of samples 1A-1D. Coloured paper sheets are placed on top of several uncoloured, otherwise identical paper sheets. B/P indicates the intensity ratio of the Raman bands of the blue pigment (B, the agent) and paper (P, the matrix), selected from the Raman spectrum collected on the coloured sheets surface. In this set of samples, the second layer is the substrate (uncoloured paper), that is made of S2 only, and it is considered to have an "infinite" thickness. In samples 1A and 1C, paper sheet coloured with a deeper blue are present (P/B = 15.5), in samples 1B and 1D a lighter colour was used (P/B = 6). Samples 1A and 1B possess only one coloured paper sheet (thickness of 90 μm), whereas in samples 1C and 1D two paper sheets were used (total thickness of 180 μm). The detailed description about sample construction and micro-SORS measurements on this set of samples can be found in [28]. The labels of the sample are the same of the mentioned publication. Adapted with permission from Ref [28].*

Each of the N layers is characterized by uniform dye concentration i.e., $C^{S1}(z_{k-1} < z < z_k) = C_k^{S1}$. Therefore, the $H(X)$ ratio has the following expression:

$$H(X) = \frac{\sum_k^N \Gamma^0(z_{k-1},z_k)}{\sum_k^N \Gamma^X(z_{k-1},z_k)} \times \frac{\sum_k^N C_k^{S1}\Gamma^X(z_{k-1},z_k)}{\sum_k^N C_k^{S1}\Gamma^0(z_{k-1},z_k)} \qquad \text{(eq. 19)}$$

As expected, the concentration of the paper (C) simplifies in the $H(X)$ expression. The first factor in eq. 19 just depends on the scattering properties of the matrix and the second factor just depends on the concentration profile of the dye across the N layers.

We apply eq. 19 to the samples 1A-1D (Figure 4) formed by two layers. The 1st layer ($k = 1; 0 < z < L_a$) is a colored layer with two Raman scatterers (dye = $S1$ and substrate = $S2$). The 2nd layer ($k = 2;\ L_a < z < +\infty$) is just plain paper ($S2$ Raman scatterer only). With such sample structure/composition, eq. 19 becomes:

$$H(X) = \frac{\Gamma^0(0,L_a)+\Gamma^0(L_a,+\infty)}{\Gamma^X(0,L_a)+\Gamma^X(L_a,+\infty)} \times \frac{C_1^{S1}\Gamma^X(0,L_a)}{C_1^{S1}\Gamma^0(0,L_a)} = \frac{\Gamma^0(0,+\infty)}{\Gamma^X(0,+\infty)} \times \frac{\Gamma^X(0,L_a)}{\Gamma^0(0,L_a)} \qquad \text{(eq. 20)}$$

As observed in Section 3 (eq. 9, Case I) $H(X)$ does not depend on the concentration of the analyte on the surface but it does on its penetration depth, L_a. Therefore, C_1^{S1} disappears in eq. 20. This immediately tells us that $H(X)$ is the same for cases 1A and 1B (the same L_a), which instead differ from the cases 1C and 1D (1C and 1D have a double thickness compared to 1A and 1B) evidencing the ability of this technique to differentiate penetration depth as also shown in the associated experimental study [28]

$G^X(z)$ function behaves as a decreasing exponential, according to eq. 17. The value of the decay length λ of $G^X(z)$ depends on the defocusing and is steeper for low defocusing values; indeed, as discussed in Section 4, λ increases linearly with the defocusing, i.e., $\lambda = \gamma X$.

Eq. 18 allows obtaining the value of γ for a given experimental set-up. In the case analysed the half of the angular aperture of the 20X objective used for micro-SORS measurements was: $\Phi = 23.57°$. Therefore $\gamma = 0.216$.

By evaluating the integrals in Eq. 20:

$$\Gamma^X(0,\mathrm{a}) = G_0^X \int_o^a e^{-\frac{z}{\gamma(X-X_f)}} dz = G_0^X \left| -\gamma(X\text{-}X_f)\, e^{-\frac{z}{\gamma(X-X_f)}} \right|_{z=0}^{z=a} = G_0^X\, \gamma(X\text{-}X_f) \left[1 - e^{-\frac{a}{\gamma(X-X_f)}}\right]$$

(eq. 21)

we obtain:

$$H(X) = \frac{\Gamma^0(0,+\infty)}{\Gamma^X(0,+\infty)} \times \frac{\Gamma^X(0,L_a)}{\Gamma^0(0,L_a)} = \frac{1-\exp\left(-\frac{L_a}{\gamma(X\text{-}X_f)}\right)}{1-\exp\left(-\frac{L_a}{\gamma(X^0-X_f)}\right)} \qquad \text{(eq. 22)}$$

The behavior of the function $H(X)$ can be straightforwardly assessed:

$$X = X^0 \;\Rightarrow\; H(X^0) = 1; \qquad X \to +\infty \;\Rightarrow\; H(X) \to 0$$

The derivative (slope) of the function $H(X)$ is:

$$\frac{\partial H(X)}{\partial X} = \frac{-\frac{L_a}{\gamma(X\text{-}X_f)^2}\, \exp\left(-\frac{L_a}{\gamma(X\text{-}X_f)}\right)}{1-\exp\left(-\frac{L_a}{\gamma(X^0-X_f)}\right)} \qquad \text{(eq. 23)}$$

By evaluating the derivative at the initial defocusing (X^0) one obtains:

$$X = X^0 \Longrightarrow \left.\frac{\partial H(X)}{\partial X}\right|_{X^0} = -\frac{L_a}{\gamma(X^0-X_f)^2} \times \frac{\exp\left(-\frac{L_a}{\gamma(X^0-X_f)}\right)}{\left[1-\exp\left(-\frac{L_a}{\gamma(X^0-X_f)}\right)\right]} < 0 \qquad \text{(eq. 24)}$$

From eq. 4 we can deduce a first important observation: *(i) the slope in X^0 is always negative*, as also observed in experiments. Moreover, in the limit of large layer thickness ($L_a \to +\infty$) we have:

$$\lim_{L_a \to +\infty} \frac{\partial H(X)}{\partial X} = 0$$

Therefore, if $\frac{\partial H(X)}{\partial X}$ is a monotonic function (which is likely), we can state that the absolute value of the slope of $H(X)$ decreases as L_a increases. This property is proven also by the following argument. Based on the representative values of $L_a = 90\ \mu\mathrm{m}, \gamma = 0.216, (X^0 - X_f) = 50\ \mu\mathrm{m}$, we deduce that $\frac{L_a}{\gamma(X^0-X_f)}$ is large

($\frac{L_a}{\gamma(X^0-X_f)}$ ~10). Hence, we can further simplify the expression of the slope at X^0, under the assumption that $\exp\left(\frac{L_a}{\gamma(X^0-X_f)}\right) \gg 1$, since $\frac{L_a}{\gamma(X^0-X_f)}$ ~10.

$$\left.\frac{\partial H(X)}{\partial X}\right|_{X^0} = -\frac{L_a}{\gamma(X^0-X_f)^2} \times \frac{\exp\left(-\frac{L_a}{\gamma(X^0-X_f)}\right)}{\left[1-\exp\left(-\frac{L_a}{\gamma(X^0-X_f)}\right)\right]} \sim$$

$$\sim -\frac{L_a}{\gamma(X^0-X_f)^2} \times \frac{1}{\left[\exp\left(\frac{L_a}{\gamma(X^0-X_f)}\right)-1\right]} \sim -\frac{L_a}{\gamma(X^0-X_f)^2}\exp\left(-\frac{L_a}{\gamma(X^0-X_f)}\right) \quad \text{(eq. 25)}$$

This expression implies that $\left.\frac{\partial H(X)}{\partial X}\right|_{X^0}$ decreases (in absolute value) with increasing L_a.

Hence, we obtained a second important general consideration: *(ii) the higher is the penetration depth of the analyte (larger L_a) the lower is the absolute value of the slope of the the normalized intensity ratio $H(X)$*. This behaviour is illustrated in Figure 5, which shows the trend of $H(X)$, calculated according to eq. 22, while varying the value of L_a

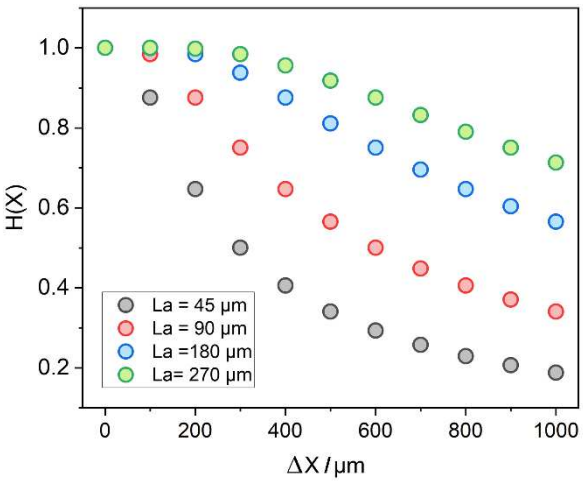

Figure 5. *Calculated $H(X)$ values (eq. 22) plotted vs $\Delta X = (X - X_f)$, for samples characterized by different penetration depth L_a. L_a varies from 45 to 270 µm.*

Indeed, the experimental data for cases 1A and 1B (90 µm layer thickness, see Figure 4) showed that the absolute value of the slope was higher than for 1C and 1D scenarios (180 µm layer thickness) (see [28] and Table 1).

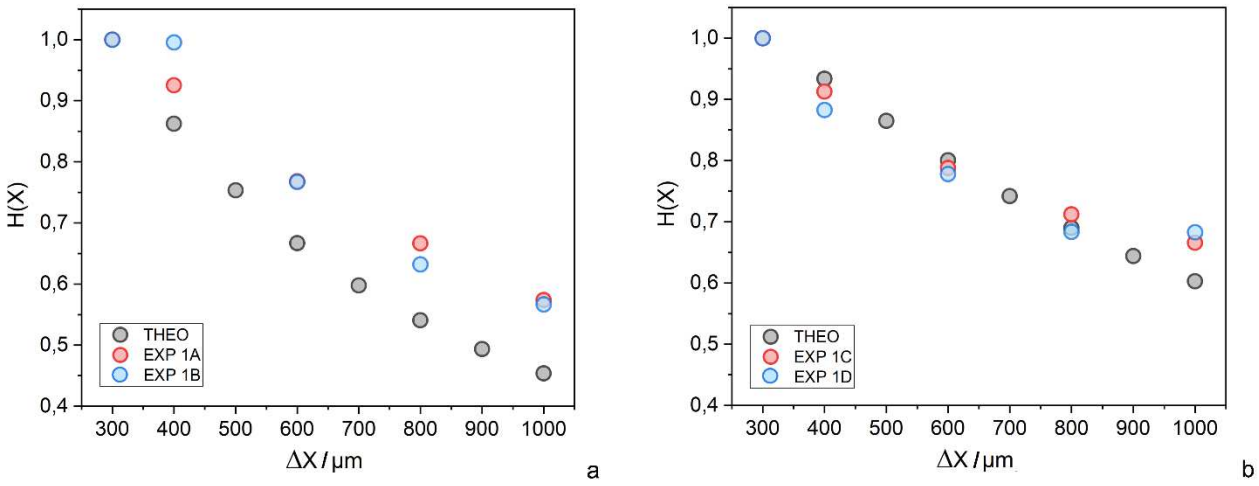

Figure 6. *Normalized micro-SORS ratios for samples 1A-1B (panel a) and 1C-1D (panel b), plotted vs* $\Delta X = (X - X_f)$. *Experimental data: red and light blue circles;* [28] *prediction according to eq. 22: grey circles. Micro-SORS ratios are normalized to the reference defocusing distance* $(X_0 - X_f)$ *= 300 μm.*

The plots in Figure 6 compare $H(X)$ obtained from experimental spectra [28] with values calculated according to eq. 22. The agreement is very good, especially if one considers that no adjustable fitting parameters are introduced: the predicted $H(X)$ values depend only on the sample parameter L_a , i. e. the penetration depth of the dye, with the γ parameter being completely independent of the sample. Indeed, γ is obtained by means of MC modelling of the propagation of photons in a turbid medium (Section 4) and it is valid (within the approximations adopted) for any sample.

In particular, the plot obtained through eq. 22 gives a surprisingly good fit of the experimental data for sample 1C and 1D (Figure 6b). Moreover, the experimental trend of the slopes of $H(X)$, obtained through a linear fitting of $H(X)$ in the range 300 - 1000 μm is also well reproduced by our prediction (Table 1).

Conclusions

The physical model developed here provides an important theoretical basis for the interpretation of a recently developed application of micro-SORS for the study of distribution of diffusing agent into a matrix, by means of analytical expressions where the basic characteristic parameters of the sample are explicitly considered (*i.e.,* analyte concentrations and analyte penetration depths). As summarized in Table 2, the derived equations put into light which physical quantities affect the $H(X)$ and $R(X)$ trends measured by micro-SORS experiments.

The model allows to properly rationalise the observed decreasing trend of the normalized micro-SORS intensity ratios ($H(X)$) with increasing defocusing distance in simple layered samples, where the agent is localized on a layer of finite thickness. The $H(X)$ trend obtained with the model is fully consistent with the measured trend; moreover, the model demonstrates that the $H(X)$ slope, $dH(X)/dX$, is a good parameter for characterizing the penetration depth of the agent. The model also highlights that the normalization procedure introduced in the definition of $H(X)$ makes the $H(X)$ trends independent from the value of the concentration of the agent on the surface (and from the laser power incident on the sample), but makes *H(X)* sensitive to the concentration gradient. This is fully consistent with what is observed in micro-SORS experiments.

The model was developed to be applicable to real situations encountered in Cultural Heritage, but its use can be extended to materials of interest in several other contexts, such as biomedical field, solar cells and semiconductors technologies. [39]

Based on the encouraging results obtained through the direct comparison between the prediction of the model and the experimental data, we believe that the general equation (eq. 8) and the related expression for layered systems (eq. 10) are a useful tool that can support the interpretation of micro-SORS data of complex samples.

Moreover, we proven that the Monte Carlo modelling of the photon propagation in non-transparent media provides a convenient universal analytical expression, which allows describing the variation of the Raman response of the analyte by the effective ability to collect Raman photons generated at different depths inside a turbid sample.

References

1. Ye, L.; de Jong, M. P.; Kudernac, T.; van der Wiel, W. G.; Huskens, J. *Mater. Sci. Semicond. Process*. **2017**, 62, 128-134

2. Bansal, N.; Gupta, M.; Mohanty, B. C.; Singh, K. *J. Am. Ceram. Soc.* **2021**, 104, 851-859

3. Andersson, J.; Rosenholm, J.; Areva, S.; Lindèn, M. Influences of Material Characteristics on Ibuprofen Drug Loading and Release Profiles from Ordered Micro- and Mesoporous Silica Matrices. *Chem. Mater*. **2004**, 16, 4160-4167

4. Yahya, I.; Atif, R.; Ahmed, L.; Eldeen, T. S.; Omara, A.; Eltayeb, M. Mathematical Modeling of Diffusion Controlled Drug Release Profiles from Nanoparticles. *Int. j. res. sci. innov*. **2019**, 6, 287-291

5. Colombo, P.; Bettini, R.; Catellani, P. L.; Santi, P.; Peppasa, N. A. Drug volume fraction profile in the gel phase and drug release kinetics in hydroxypropylmethyl cellulose matrices containing a soluble drug. *Eur. J. Pharm. Sci.* **1999**, 9, 33–40

6. Schulz, R.; Yamamoto, K.; Klossek, A.; Rancan, F.; Vogt, A.; SchÜtte, C.; RÜhl, E.; Netz, R. R. Modeling of Drug Diffusion Based on Concentration Profiles in Healthy and Damaged Human Skin. *Biophys. J.* **2019**, 117, 998–1008

7. Molina, E.; Rueda-Quero, L.; Benavente, D.; Burgos-Cara, A.; Ruiz-Agudo, E.; Cultrone, G. Gypsum crust as a source of calcium for the consolidation of carbonate stones using a calcium phosphate-based consolidant. *Constr. Build. Mater*. **2017**, 143, 298-311

8. Conti, C.; Colombo, C.; Festa, G.; Hovind, J.; Perelli Cippo, E.; Possenti, E.; Realini, M. Investigation of ammonium oxalate diffusion in carbonatic substrates by neutron tomography. *J. Cult. Herit*. **2016**, 19, 463 - 466

9. Realini, M.; Colombo, C.; Conti, C.; Grazzi, F.; Perelli Cippo, E.; Hovind, J. Development of neutron imaging quantitative data treatment to assess conservation products in cultural heritage. *Anal. Bioanal. Chem*. **2017**, 409, 6133-6139

10. Conti, C.; Colombo, C.; Dellasega, D.; Matteini, M. ; Realini, M.; Zerbi, G. Ammonium oxalate treatment: evaluation by μ-Raman mapping of the penetration depth in different plasters. *J. Cult. Herit.* **2011**, 12, 372-379.

11. Conti, C.; Colombo, C.; Matteini, M.; Realini, M. ; Zerbi, G. Micro-Raman mapping on polished cross sections: a tool to define the penetration depth of conservation treatment on cultural heritage. *J. Raman Spectrosc.* **2010**, 41, 1254-1260

12. Conti, C.; Aliatis, I.; Colombo, C.; Greco, M.; Possenti, E.; Realini, M.; Castiglioni, C.; Zerbi, G. μ-Raman mapping to study calcium oxalate historical films. *J. Raman Spectrosc*. **2012**, 43, 1604-1611.

13. Calore, N.; Botteon, A.; Colombo, C.; Comunian, A.; Possenti, E.; Realini, M.; Sali, D.; Conti, C. High Resolution ATR μ-FTIR to map the diffusion of conservation treatments applied to painted plasters. *Vib. Spectrosc.* **2018,** 98, 105-110

14. Casadio, F.; Toniolo, L.; Polymer Treatments for Stone Conservation: Methods for Evaluating Penetration Depth, *J. Am. Inst. Conserv*. **2004**, 43, 3-21

15. Pinto, A.P.F.; Rodrigues, J.D. Consolidation of carbonate stones: Influence of treatment procedures on the strengthening action of consolidants. *J. Cult. Heritage*, **2012**, *13*, 154-166

16. Carmona-Quiroga, P.M.; Martínez-Ramírez, S.; Sánchez-Cortés, S.; Oujja, M.; Castillejo, M.; Blanco Varela, M.T. Effectiveness of antigraffiti treatments in connection with penetration depth determined by different techniques. *J. Cult. Herit*. **2010**, *11*, 297-303

17. Graziani, G.; Colombo, C.; Conti, C.; Possenti, E.; Cippo, E.P.; Realini, M.; Sassoni, E. Neutron radiography as a tool for assessing penetration depth and distribution of a phosphate consolidant for limestone. *Constr. Build. Mater*. **2018**, *187*, 238-247.

18. Graziani, G.; Sassoni, E.; Scherer, G.W.; Franzoni, E. Penetration depth and redistribution of an aqueous ammonium phosphate solution used for porous limestone consolidation by brushing and immersion. *Constr. Build. Mater*. **2017**, *148*, 571-578.

19. Franzoni, E.; Sassoni, E.; Graziani, G. Brushing, poultice or immersion? The role of the application technique on the performance of a novel hydroxyapatite-based consolidating treatment for limestone. *J. Cult. Herit*. **2015**, 16, 173-184

20. Osticioli, I.; Botticelli, G.; Matteini, P.; Siano, S.; Pini, R.; Matteini, M. Micro-Raman analysis on the combined use of ammonium oxalate and ammonium phosphate for the consolidation and protection of carbonate stone artifacts. *J. Raman Spectrosc*. **2017**, *48*, 966-971

21. Ban, M.; Aliotta, L.; Gigante, V.; Mascha, E.; Sola, A.; Lazzeri, A. Distribution depth of stone consolidants applied on-site: Analytical modelling with field and lab cross-validation. *Constr. Build. Mater*. **2020**, *259*, 120394

22. Mudronja, D.; Vanmeert, F.; Fazinic, S.; Janssens, K.; Tibljas, D.; Desnica, V. Protection of Stone Monuments Using a Brushing Treatment with Ammonium Oxalate. *Coatings* **2021**, 11, 379.

23. Possenti, E.; Conti, C.; Gatta, G.D.; Merlini, M.; Realini, M.; Colombo, C. Synchrotron radiation μ X-ray diffraction in transmission geometry for investigating the penetration depth of conservation treatments on cultural heritage stone materials. *Anal. Methods* **2020**, 12, 1587-1594.

24. Prudêncio, M.I.; Pereira, M.S.; Marques, J.G.; Dias, M.I.; Esteves, L.; Burbidge, C.I.; Trindade, M.J.; Albuquerque, M.B. Neutron tomography for the assessment of consolidant impregnation efficiency in Portuguese glazed tiles (16th and 18th centuries). *J. Archaeol. Sci.* **2012**, *39*, 964-969

25. Jia, Y.; Sciutto, G.; Mazzeo, R.; Samorì, C.; Focarete, M.L.; Prati, S.; Gualandi, C. Organogel Coupled with Microstructured Electrospun Polymeric Nonwovens for the Effective Cleaning of Sensitive Surfaces. *ACS appl. Mater. Interfaces* **2020**, *12*, 39620-39629

26. Botteon, A.; Yiming, J.; Prati, S.; Sciutto, G.; Realini, M.; Colombo, C.; Castiglioni, C.; Matousek, P.; Conti, C. Non-invasive characterisation of molecular diffusion of agent into turbid matrix using micro-SORS. *Talanta* **2020**, 218, 121078

27. Jia, Y.; Sciutto, G.; Botteon, A.; Conti, C.; Focarete, M.L.; Gualandi, C.; Samorì, C.; Prati, S.; Mazzeo, R. Deep eutectic solvent and agar: a new green gel to remove proteinaceous-based varnishes from paintings. *J. Cult. Herit*. **2021**, 51, 138-144

28. Botteon, A.; Realini, M.; Colombo, C.; Conti, C.; Matousek, P.; Castiglioni, C. Micro-SORS, diffusion processes and heritage science: a non-destructive and systematic investigation *Eur. Phys. J. Plus* **2021***,* 136, 880

29. Mosca, S.; Conti, C.; Stone, N.; Matousek, P. Spatially offset Raman spectroscopy. *Nat. Rev. Methods Prim*. **2021**, 1, 22

30. Conti, C.; Colombo, C.; Realini, M.; Zerbi, G.; Matousek, P. Subsurface Raman Analysis of Thin Painted Layers. *Appl. Spectrosc*. **2014**, 68, 686-691

31. Conti, C.; Realini, M.; Colombo, C.; Matousek, P. Comparison of key modalities of micro-scale spatially offset Raman spectroscopy. *Analyst*, **2015**, 140, 8127-8133

32. Matousek, P.; Morris, M.D.; Everall, N.; Clark, I.P.; Towrie, M.; Draper, E.; Goodship, A.; Parker, A.W. Numerical simulations of subsurface probing in diffusely scattering media using spatially offset Raman spectroscopy. *Appl. Spectrosc.* **2005**, *59*, 1485-1492

33. Conti, C.; Realini, M.; Colombo, C.; Matousek, P. Comparison of key modalities of micro-scale spatially offset Raman spectroscopy. *Analyst*, **2015**, 140, 8127-8133

34. Di, Z.; Hokr, B.H.; Cai, H.; Wang, K.; Yakovlev, V.V.; Sokolov, A.V.; Scully, M.O. Spatially offset Raman microspectroscopy of highly scattering tissue: theory and experiment. *J. Mod. Opt.* **2015**, 62, 97-101

35. Matousek, P.; Conti, C.; Colombo, C.; Realini, M. Monte Carlo simulations of subsurface analysis of painted layers in micro-scale spatially offset Raman spectroscopy. *Appl. Spectrosc.* **2015**, 69, 1091-1095

36. Conti, C.; Botteon, A.; Colombo, C.; Realini, M.; Matousek, P. Fluorescence suppression using micro-scale spatially offset Raman spectroscopy. *Analyst*, **2016**, 141, 5374-5381

37. Das, B.B., Liu, F. and Alfano, R.R. Time-resolved fluorescence and photon migration studies in biomedical and model random media. *Rep. Prog. Phys*. **1997**, 60, 227.

38. Mosca, S.; Dey, P.; Salimi, M.; Gardner, B.; Palombo, F.; Stone, N.; Matousek, P. Spatially Offset Raman Spectroscopy—How Deep?. *Anal. Chem.* **2021**, 93, 6755-6762

39. Botteon, A.; Kim, W.-H.; Colombo, C.; Realini, M.; Castiglioni, C.; Matousek, P.; Kim, B.-M.; Kwon, T.-H.; Conti, C. Non-destructive Monitoring of Dye Depth Profile in Mesoporous TiO_2 Electrodes of Solar Cells with Micro-SORS. *Anal. Chem*. **2022**, In press, https://doi.org/10.1021/acs.analchem.1c05011

Table 1. L_a of samples 1A-1B and 1C-1D and absolute value of the slope of the $H(X)$ function determined experimentally and with eq. 22. The slopes are obtained through a linear fitting of $H(X)$ in the range 300 - 1000 µm.

Sample	L_a (µm)	H slope (exp) µm^{-1}	H slope (model) µm^{-1}
1A	90	6 x 10^{-4}	8 x 10^{-4}
1B	90	7 x 10^{-4}	8 x 10^{-4}
1C	180	5 x 10^{-4}	6 x 10^{-4}
1D	180	5 x 10^{-4}	6 x 10^{-4-}

Table 2. *Physical factors that influence the micro-SORS ratios ($R(X)$ and normalized ratios $H(X)$ in a turbid sample with concentration profiles $C^{Sk}(z)$ of two analytes with depth.*

physical quantity	$R(X)$	$H(X)$	comment
σ^{S1}, σ^{S2}	YES	NO	the ratio of the absolute Raman cross sections is present in the expression $R(X)$
$C^{S1}(z)$, $C^{S2}(z)$	YES	YES	
laser power	NO	NO	
λ_{laser}	YES	NO	λ_{exc} modifies σ^{S1}, σ^{S2}
photon propagation: reduced scattering coefficient (μ_s')	YES	YES	- but negligible dependence in high turbidity regime (photon transport length << laser beam diameter) / through $G^X(z)$ – universal expression deduced through MC simulation + experimental parameter, i.e. objective semi-aperture - negligible absorption assumed
penetration depth (L_a)	YES	YES	special case: $C^{S1}(z) = C \;\; for \;\; 0 < z \leq L_a;$ $C^{S1}(z) = 0 \quad if \; z > L_a$